Progress Toward the Critical Design of the Superconducting Rotor for NASA's 1.4 MW High-Efficiency Electric Machine

Justin J. Scheidler* and Thomas F. Tallerico†
NASA Glenn Research Center, Cleveland, Ohio, 44135

Wesley A. Miller‡
Vantage Partners, Cleveland, Ohio, 44142

William Torres§
Wolf Creek Federal Services, Cleveland, Ohio, 44135

NASA Glenn Research Center is developing a 1.4 MW high-efficiency electric machine for future electrified aircraft. This wound-field, synchronous machine employs a self-cooled, superconducting rotor to achieve excellent specific power and efficiency. This paper presents the progress made over the past year toward a critical design of the superconducting rotor, including refined analysis and risk reduction testing on prototype superconducting coils. A 3D finite element model of the rotor is developed to simulate the combined loading imposed by the initial cool down of the rotor from room temperature to cryogenic temperature and the subsequent rotation of the rotor up to the design speed. The model is evaluated to better predict the stress state in the critical components and the reduction in physical gap between the stator and rotor due to the resulting radial deflections. This model includes an enhanced model of the superconducting coil that considers the coil as an assembly of four individual coil layers. An improved coil fabrication process is described in detail. Two sub-scale test coils are fabricated and then tested under repeated thermal cycling between room temperature and liquid nitrogen temperature (77 K). It is demonstrated that the proposed coil fabrication procedure can produce no-insulation, high temperature superconducting coils that can survive several thermal cycles without apparent degradation.

I. Introduction

To drastically reduce the energy consumption, emissions, and noise of future commercial transport aircraft, NASA is investing in a broad portfolio of enabling research and development for electrified aircraft propulsion (EAP) [1]. A number of transport aircraft concepts that harness EAP have been shown to provide system-level benefits to energy consumption, fuel burn, and/or emissions [2–8]. As expected, the existence of the benefits and their magnitude depend on the assumed performance of the individual EAP components. Two of the more influential characteristics are the specific power and efficiency of the EAP system's electric machines. Specific power several times greater than industrial motors and efficiency at or above the state of the art (96%) are typically needed for an aircraft concept to be promising [9, 10]. Accordingly, NASA's EAP investment includes the development of three megawatt-class electric machines that each combine high electromagnetic specific power (>13 kW/kg) with high efficiency (>96%) [1].¶ NASA Glenn Research Center is developing a 1.4 MW wound-field synchronous machine. The machine is referred to as the high-efficiency megawatt motor (HEMM) [11]. To illustrate the effect of this machine on a transport aircraft with EAP, system-level studies were performed for one concept aircraft, the NASA single-aisle turboelectric aircraft with aft boundary layer propulsor (STARC-ABL). Recent, refined analyses of this concept indicate that it can provide a fuel savings of up to 4% when compared to a future vehicle with assumed technology advancement. Prior to this recent analysis, a comparative study was conducted to quantify the system-level benefits to STARC-ABL of using HEMM (goals: 16 kW/kg, 98%

---

*Research Mechanical Engineer, Rotating and Drive Systems Branch, 21000 Brookpark Road, Cleveland, Ohio, 44135, non-member.

†Research Engineer, Rotating and Drive Systems Branch, 21000 Brookpark Road, Cleveland, Ohio, 44135, non-member.

‡Electrical Engineer, 3000 Aerospace Pkwy, Brookpark, Ohio, 44142, non-member.

§Electrician, 21000 Brookpark Road, Cleveland, Ohio, 44135, non-member.

¶For transport aircraft up to the single-aisle class, a megawatt-level continuous power rating permits the use of several different EAP configurations (e.g., parallel hybrid, partially turboelectric, or fully turboelectric).

to 99%) instead of a future electric machine that meets the performance targets established by NASA (13 kW/kg, 96%). For the STARC-ABL revision A analysis, HEMM enabled a 1.5% to 2.5% reduction in fuel burn on top of the reduction that this future electric machine provided (7% to 10% [7]) [1]. A potentially more impactful benefit of HEMM is that, relative to this future electric machine, it would reduce the electric machines' waste heat by 50% to 75%. This reduction in waste heat would decrease the size and mass of the EAP system's thermal management hardware.

The exceptional specific power and efficiency of the HEMM is primarily achieved by utilizing a slotless stator and a self-cooled, superconducting rotor. A superconducting field winding has a negligible amount of internal energy loss‖ and can produce magnetic field strengths that greatly exceed those produced by conventional conductors or permanent magnets. However, the use of superconductors introduces a number of challenges. Superconductors must be kept at cryogenic temperatures and the superconducting system must be carefully designed to avoid a loss of superconductivity, which will occur when the temperature, magnetic flux density, or conduction current in the superconductor exceed design limits. Additionally, superconductors are fragile compared to copper and aluminum conductors; superconductors are subject to maximum strain and minimum bend radius constraints, and care must be taken to avoid appreciable shear stresses and transverse tensile stresses. Superconductors are also significantly more expensive than copper and aluminum conductors. Consequently, it is important to conduct analysis and sub-scale testing prior to full-scale implementation to reduce these risks.

This paper discusses the progress made over the past year toward a critical design of the superconducting rotor for the HEMM. Progress was made in two areas: (1) the design was refined by performing a more detailed analysis that eliminated two of the key simplifications used in the preliminary design phase and (2) a collection of thermal cycling tests were performed on prototype coils to reduce the risks associated with thermal stresses. Section II summarizes the overall design of HEMM's superconducting rotor. Section III presents the refined finite element analysis. Section IV describes the test setup and results of the risk reduction testing. Finally, the conclusions are summarized in Section V.

II. Summary of the design of the HEMM's rotor

The preliminary design of the HEMM's superconducting rotor was detailed in [12] and [13]. Figure 1 depicts the current design of the superconducting rotor and Table 1 summarizes the notable characteristics. The design of the superconducting coils' structural containment is unique due to the large number of rotor poles (12) and the desire to maximize the electromagnetic performance. The performance was maximized by minimizing the air gap between the rotor and stator and moving the coils outward toward the surface of the rotor as much as possible.
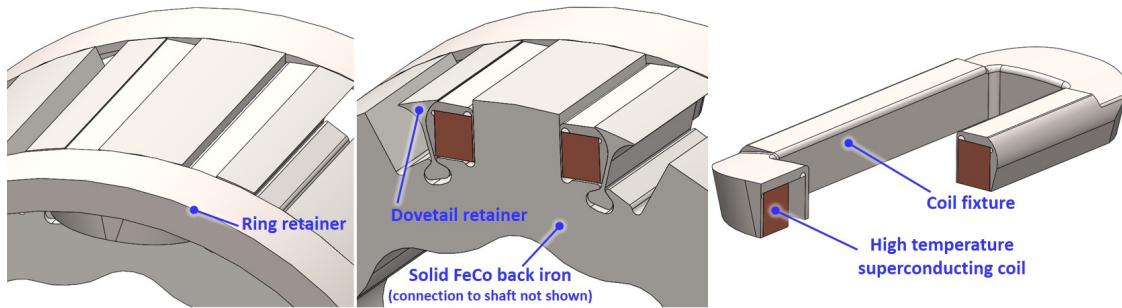

Fig. 1 Design of the superconducting rotor, showing 1 of the 12 superconducting coils.

The objective of the field windings on the rotor of an electric machine is to magnetize the stator and generate the largest possible magnetic flux density in and around the stator windings. The HEMM uses superconducting field windings to greatly increase this magnetic excitation for the benefit of increased specific power and efficiency. One of the aforementioned challenges with using superconductors is quench, or a loss of superconductivity as a result of excessive temperature, magnetic flux density, or conduction current in the superconductor. Although this issue is typically mitigated by limiting the applied current to a fraction of the superconducting coil's critical current, quench may still occur due to a number of reasons, such as inaccuracies in the analysis, unexpected heat sources, or transients

---

‖Not including the conventional conductors that supply the superconductor with current from room temperature, a superconducting winding only exhibits loss due to the resistive splice joints between superconductor segments and AC losses caused by alternating conduction current and/or alternating external magnetic flux.
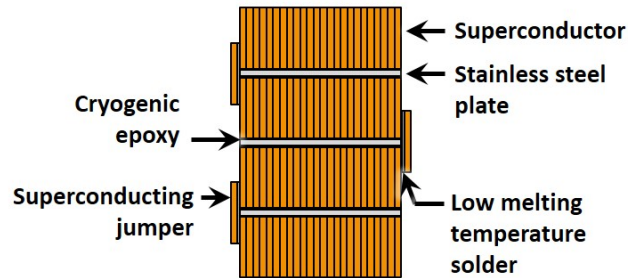
Table 1   Key characteristics and geometry of the HEMM's superconducting rotor.

Characteristic/parameter	Value	Characteristic/parameter	Value
Rotation speed, rpm	6,800	Superconductor width, mm	4
Electrical frequency, Hz	DC	Superconductor thickness, μm	65
Number of poles	12	Min. superconductor bend radius, mm	15
Stator configuration	semi-slotless	Max. magnetic flux density in the superconductor, T	2
Rotor outside diameter, cm	30	Superconductor operating temperature, K	<63
Rotor/stator axial length, cm	12.5	Superconductor DC operating current, A	51.5
Radial air gap, mm	3		

in the operating state. Consequently, controllers are often used to monitor the state of the coil and rapidly reduce the current when quench is detected.

An alternative method of quench protection is to remove the turn-to-turn electrical insulation from the coil [14]. This method provides inherent quench protection by allowing the applied current to flow around a normal (i.e., non-superconducting) region in the superconductor. Other benefits of so-called no-insulation coils include higher engineering current density, better mechanical strength, and resistance to defects in the superconductor. The downside of no-insulation coils is that they exhibit a charging delay (i.e., the magnetic field produced by the coil lags in time behind the applied current). However, this is a minimal concern for the field winding of an electric machine, because the applied current is DC and the time constants of the charging delay are typically small (on the order of seconds or less). Therefore, no-insulation coils were selected for the rotor of the HEMM.

The selected 2nd generation high-temperature superconductor (HTS) is the REBCO (rare-Earth barium copper oxide) material, which is commercially available in long piece lengths that provide sufficient performance at high temperatures (about 77 K and below) and in moderately strong magnetic excitations. The conductor has a rectangular cross-section that permits a very high packing factor of turns within a given volume. The HEMM's rotor coils have a racetrack shape and a cross-sectional geometry that was optimized for maximum magnetic flux density per mass, subject to the superconductor's magnetic flux density limit listed in Table 1 [12]. The coil's cross section, shown in Figure 2, is composed of four layers, or individual pancake/racetrack coils, that each contain about 230 turns and are electrically connected in series using pieces of the same HTS. The layers are bonded together using a cryogenic epoxy. A thin stainless steel plate with the same planar geometry is bonded between each layer and on top of the coil to provide mechanical support and to axially align the individual turns in each layer.

Fig. 2   Schematic of the cross-sectional geometry of HEMM's rotor coils (not to scale).

III. Refined finite element analysis

This section presents the results of a refined finite element analysis (FEA) of the HEMM's rotor. At the preliminary design stage, a number of simplifications were made to expedite the down selection of candidate designs [12]. Two key simplifications were (a) neglecting the thermally-induced stresses in the superconducting coil and (b) modeling the

coil as a single, solid block of copper. In the updated analysis below, these simplifications were removed. A 3D finite element model of the rotor is developed to simulate the combined loading imposed by the initial cool down of the rotor from room temperature to cryogenic temperature and the subsequent rotation of the rotor up to the design speed. The model is evaluated to better predict the stress state in the critical components and the reduction in physical gap between the stator and rotor due to the resulting radial deflections.

An enhanced model of the superconducting coil is included that considers the coil as an assembly of four individual, solid layers separated by thin plates rather than as a single, solid block of copper. Ideally, each turn of the coil would be explicitly modeled with mechanical contact boundary conditions between neighboring turns. However, such a model is computationally impractical and it may be impossible in practice for the solver to converge on a solution. Consequently, each layer of the coil is treated as a solid body having material properties that approximate the collective behavior of the many turns. A transversely isotropic shear modulus is used for each layer to approximate a coil layer's minimal shear stiffness in directions that tend to slide the turns relative to each other. An attempt was made to include a transversely isotropic Young's modulus that depends on the elastic strain such that under compression its value equals the conductor's modulus and under tension it equals the modulus of the cryogenic epoxy. Such a Young's modulus could approximate the mechanical contact between turns without explicitly modeling each turn. A converged solution could not be obtained using this approach. Thus, an isotropic Young's modulus is used here. Table 2 tabulates the mechanical material properties of the HTS coil layers that were used in this analysis.

Table 2   Mechanical material properties of the superconducting coil layers used in this analysis; E, ν, and G denote the Young's moduli, Poisson's ratios, and shear moduli where the 1-direction coincides with the superconductor's out-of-plane direction (i.e., its c-axis).

E_1, E_2, GPa	E_3, GPa	ν_{12}	ν_{23}, ν_{13}	G_{12}, GPa	G_{23}, G_{13}, GPa
150	150	0.32	0.32	56.8 $(= 0.5E_1/(1 + \nu_{12}))$	3.5

The thermally-induced stresses in the coil and thermal contraction of the rotor are appreciable due to the 230 K decrease in temperature when the HEMM's rotor is cooled down from room temperature to its operating temperature (about 60 K). This thermal contraction of the rotor and the rotor's growth due to centrifugal loading are important for defining the physical gap between the machine's rotor and stator. This behavior was accurately captured by sequentially simulating the cool down and rotation in a commercial multiphysics FEA software. To ensure continuity, the final state from the cool down study was used as the initial state of the rotation study. Sample analysis results are shown below in Fig. 3 and Fig. 4. Relative to the room temperature geometry of the assembled rotor, the outermost point on the outer surface of the 60 K rotor is deflected 0.25 mm inward toward the rotation axis (Fig. 3a). Then, as the cold rotor rotates up to the design speed of 6,800 rpm, its outermost point moves outward by about 0.33 mm to an absolute position of 0.08 mm outward from the rotor's surface at room temperature (Fig. 3b). By combining this net radial deflection of the rotor with the maximum expected deflection due to rotational unbalance, the maximum expected assembly tolerance, and a safety factor, the nominal gap between the rotor and stator can be properly sized to prevent contact.

The distribution of thermal stress is shown in Fig. 4a. Thermal stresses are low throughout most of the rotor. Due to the assumed bonding between the separating plates and coil layers and the mismatch in thermal contraction between the two materials, the thermal stress in the separating plates is moderate. For the same reason and due to its anisotropic thermal contraction, the thermal stress in the superconducting coil layers is also moderate, although primarily just in the end turns. Stresses due to centrifugal forces are considerably larger, although they are primarily contained to the titanium structural components, as desired. Table 3 compares the maximum von Mises stress in each component as calculated by an earlier FEA model that only included rotation and the improved FEA model that considers the initial cool down and subsequent rotation. Minimal differences are observed between the two models in terms of maximum von Mises stress. However, the improved model captures the increased peak stress and distribution of stress in the end turns that results from the thermal forces. The original model also greatly overpredicts the outward radial displacement of the outermost point on the rotor's surface under centrifugal loading (original model: 0.32 mm; improved model: 0.08 mm).

The dovetail retainers' maximum von Mises stress exceeds the material's yield strength. Previous analysis of a very similar design indicated a positive margin of safety when a 1.5 factor of safety is applied. In the present analysis, this peak stress is highly localized at the sharp ends of the dovetail (on the part's axial face) where it contacts the back iron, as shown in Fig. 5. It is thought that the previous analysis missed this stress due to insufficient mesh refinement at that location and a less accurate contact pressure distribution over the entire contact between the dovetail retainer and the
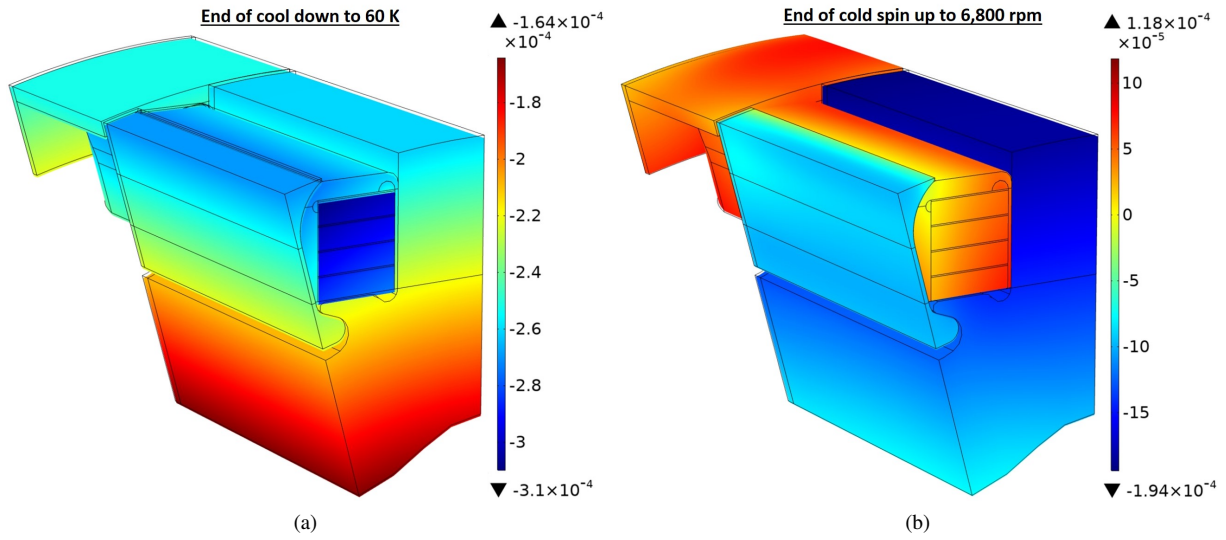
Fig. 3 Finite element analysis results of the radial deformation (in units of m) for (a) the thermal contraction of the rotor due to a uniform cool down from room temperature to 60 K and (b) the subsequent expansion caused by a cold spin up to the design speed of 6,800 rpm.
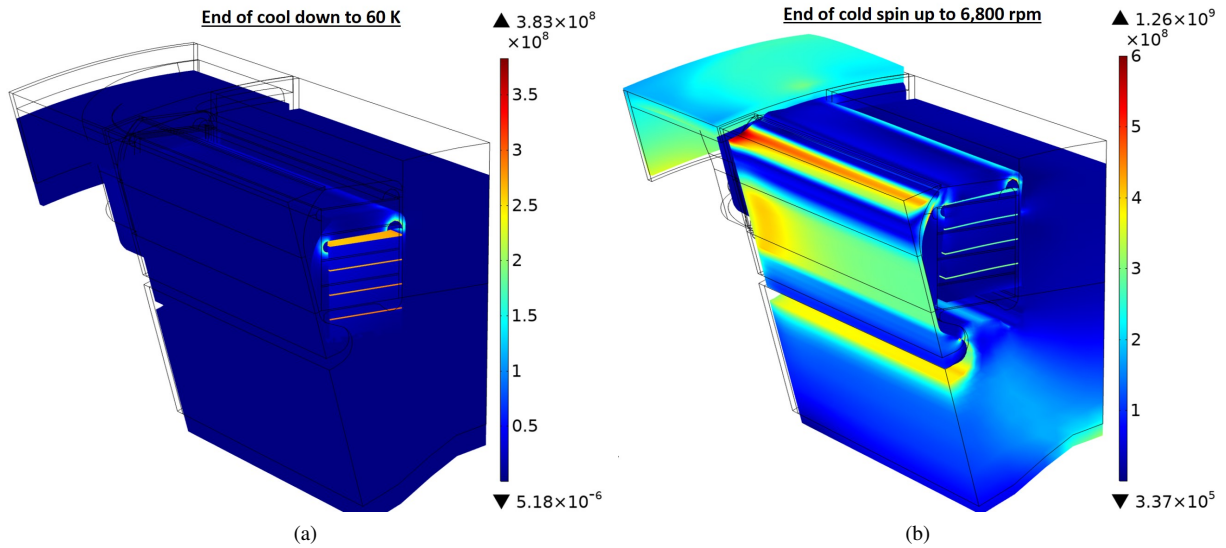

Fig. 4 Finite element analysis results of the von Mises stress (in units of Pa) for (a) the cool down of the rotor from room temperature to 60 K and (b) rotation up to the design speed of 6,800 rpm.

back iron. This excessive stress will be addressed before the critical design is finalized. It is expected that rounding the sharp edge will eliminate the stress concentration, enable a more accurate contact solution, and bring the peak stress down to the level observed away from the sharp edge (about 800 MPa).

Due to the anisotropic geometry and mechanical properties of the high temperature superconductor, it can be misleading to only consider the von Mises stress in the coil. Consequently, the stress components are tabulated in Table 4 for the operating points where the rotor has cool down to 60 K and where the cold (60 K) rotor is spun up to full speed. A failure limit is not known for many of the stress components at either cryogenic temperatures or room temperature. However, the tensile strength of the conductor is well known, and it is known that the failure strength is very low for stresses that tend to separate the superconductor film from its substrate. All of the stress components seem

Table 3 **Comparison of the max von Mises stress (in units of MPa) in each component of the rotor calculated by an earlier FEA model that includes rotation only and the improved FEA model that includes initial cool down and subsequent rotation.**

Component	Rotation-only FEA model	Cool down + rotation FEA model	Percent change	'Failure' strength, MPa
Superconducting coil	124	127	+2.4%	see Table 4
Back iron	436	433	−0.7%	694**
Coil fixture	519	507	−2.3%	1100
Dovetail retainer	1260	1260	0%	1100
Ring retainer	349	368	+5.4%	1100

**This value is an estimate of the brittle failure strength of the $Fe_{49.19}Co_{48.75}V_{1.90}$ material at 77 K. The estimate is based on measurements from the literature [15] and the manufacturer's room temperature properties.
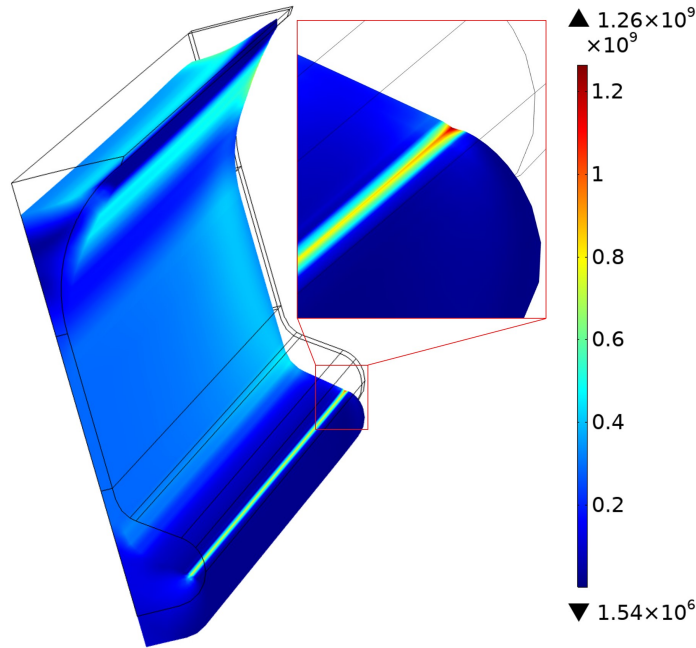

Fig. 5 **Finite element analysis results of the von Mises stress (in units of Pa) in the dovetail retainer at the operating temperature of 60 K and the design speed of 6,800 rpm.**

to be sufficiently low, although a more thorough evaluation is warranted for the tensile σ_{22} at both operating conditions, the tensile σ_{33} at full speed, and the σ_{12} at full speed.

IV. Risk reduction testing

This section presents the progress made in reducing the risks that the full-scale HEMM prototype will fail or be limited in performance by a problem with the superconducting rotor. These risks are described in [11].

Although they were suggested only recently, a number of papers have reported the fabrication and critical current testing of no-insulation coils [13, 14, 16, 17]. However, no-insulation coils have not been used in the rotor of an electric machine. The presence of significant centrifugal forces in the rotor of aircraft electric machines complicates the design of the no-insulation coil and its mechanical support structure. Also, nearly all no-insulation HTS coils are cooled by liquid cryogen and have a simple circular geometry. The superconducting coils in the HEMM are conductively cooled and have a racetrack geometry that complicates the thermal stress environment. Combined, these aspects pose a significant challenge for realizing the quench protection benefit of the no-insulation approach (i.e., for maintaining

Table 4   Range of stresses (in units of MPa) in the superconducting coil after cool down to 60 K and after cold spin up to 6,800 rpm; the 1-, 2-, and 3-directions correspond to the superconductor's length direction (a-axis), b-axis, and c-axis, respectively.

Stress component		'Failure' strength	End of cool down to 60 K	End of cold spin up to 6,800 rpm
Normal stress	σ_{11}	> 550	-86.1 to 63.5	-145 to 80.3
	σ_{22}	low (?) in tension	-18.8 to 27.8	-181 to 24.8
	σ_{33}	very low in tension	-37.1 to 9.8	-91.1 to 16.2
Shear stress	σ_{12}, σ_{21}	low (?)	-10.1 to 6.5	-19.8 to 40.6
	σ_{23}, σ_{32}	very low	-5.8 to 6.8	-6.0 to 12.0
	σ_{13}, σ_{31}	very low	-0.4 to 1.4	-2.1 to 2.8

adequate contact between the turns of the coil) and maintaining the integrity of the conductor. Considering the high cost of superconductors, it is therefore critically important to fabricate prototype coils and conduct risk reduction testing, starting with small, simple coils then advancing to full-scale, full-complexity coils.

To reduce the risk that the HEMM's superconducting coils will be damaged by thermal stresses, a series of thermal cycling tests have been conducted on multiple sub-scale test coils. Prior work by the authors [13] discussed the coil fabrication and testing procedures and presented initial measurements of how two small, single-layer coils responded to repeated thermal cycling between room temperature and liquid nitrogen temperature (77 K). Here, that work is expanded by describing an improved coil fabrication procedure and by presenting thermal cycling measurements of two new sub-scale coils that have nearly all of the features of the full-scale HEMM coils.

A. Improved coil fabrication procedure

After winding multiple sub-scale HTS coils using the authors' original coil fabrication process [13], the process was found to have a few deficiencies. The primary issue was that the geometry of the coils' end turns considerably deviated from the design; this resulted from the coil former's insufficient stiffness in some locations and the build up of a small amount of slack in the coil while winding. Another problem was that the finished coils had an excessive amount of epoxy where it was not desired (on the radially outer and inner faces); this was caused by a lack of accessibility to those faces and the need to avoid removing epoxy from where it is needed to hold the turns in place (the axial faces of the coil). Finally, the current terminals were unrealistic, and the superconducting current leads were used in the test setup but they aren't a part of the design.

The improved coil fabrication process described below and depicted in Figure 6 resolved the aforementioned deficiencies. First the end of the superconductor was bent and then inserted into a slot in the coil former to secure it in place (image 1). The entire coil fabrication fixture was then rotated to wind the desired number of turns onto the coil former; during this step, the superconductor was gently cleaned with alcohol as it was pulled off of its spool. The winding tension was controlled by a pneumatic tensioner (not depicted). Care was taken to maintain a constant pull in the fixture's rotation direction to minimize the amount of slack in the winding. Relative to the prior procedure, the coil former is significantly stiffer in the end turn area, particularly where the slot is, and much more of the coil's top surface and edges are exposed and accessible. Periodically while winding, the turns were gently pushed down onto the fixture's base to align them in the axial direction (image 2). Once the desired number of turns were wound, side clamps were inserted, pressed toward the rotation axis, and screwed in place to apply mild pressure on the straight sides of the racetrack (image 3). A moderate amount of cryogenic epoxy was then carefully applied onto only the exposed, top surface of the coil (image 4). A 0.254 mm thick stainless steel plate shaped like the coil was placed on top of the epoxy and pressed down to squeeze out any excess epoxy and eliminate any gap between the plate and coil. The excess epoxy was then removed from the radially outer and inner faces (image 5). Although it was added to provide mechanical support (to prevent turns from shifting), the plate was found to considerably ease the task of removing excess epoxy without having to worry about removing too much epoxy from the coil's top face where it holds the turns together. A mass was then placed on top of a coil-shaped cap that applied pressure only to the top face of the coil (image 6). The coil was again cleaned to remove any remaining excess epoxy. Then the epoxy was allowed to cure for 24 hours at room temperature. This process was repeated to produce the desired number of coil layers. The winding orientation of
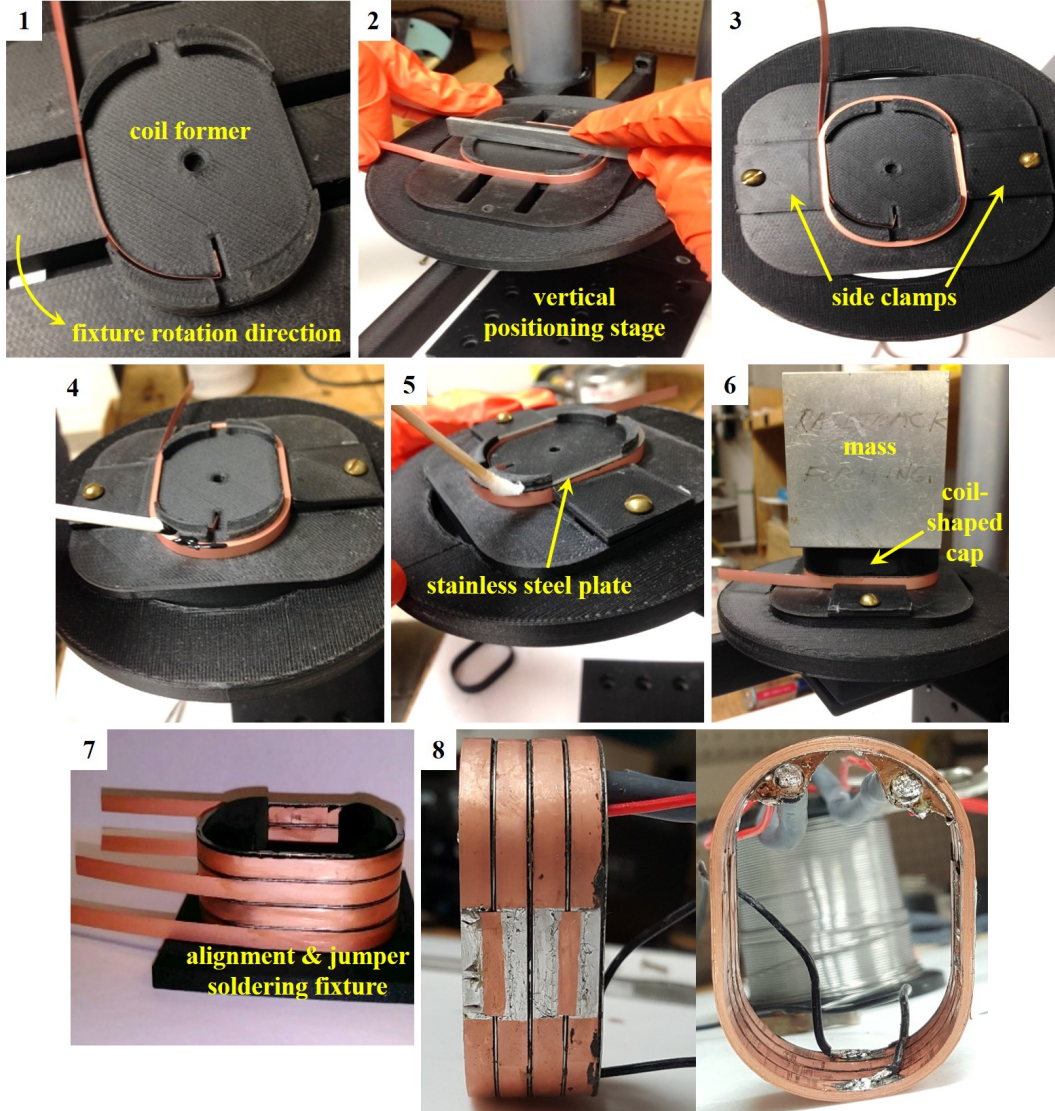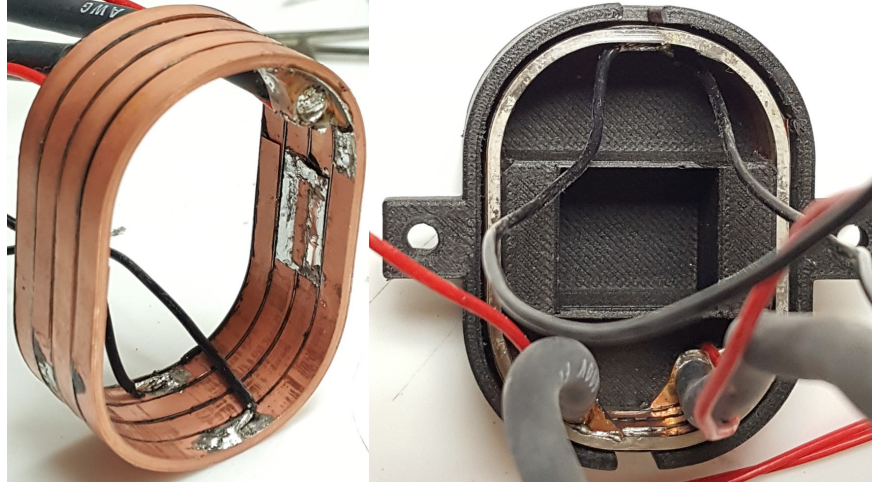
Fig. 6   Key steps in the improved procedure for fabricating superconducting rotor coils for the HEMM.

adjacent layers must be opposite to produce the required flow of current through the coil. Thus, half of the coils were wound in the opposite fixture rotation direction using a coil former that is a mirror of the one depicted in image 1. The coil layers were then placed on a separate fixture that aligned them to each other, provided access to the layer-to-layer jumper locations, and guides for correctly positioning the jumpers (image 7). Non-pre-tinned superconducting jumpers were then soldered onto the coil using a low melting temperature ribbon solder (52In 48Sn). The excess superconductor extending from the outside of each layer was then carefully cut off. A copper current lead was soldered into each copper current terminal using higher melting temperature solder (96.5Sn 3Ag 0.5Cu). The terminals were then soldered onto the coil using the same low melting temperature ribbon solder. The coil was completed by soldering on voltage taps using low melting temperature solder. A completed 4-layer sub-scale coil is shown in image 8 of Figure 6.

Multiple 2-layer and 4-layer sub-scale coils were fabricated using this improved process. Figure 7 depicts one of these 4-layer coils along with a 2-layer coil that was fabricated using the original procedure. The section that follows presents thermal cycling data for both of these coils.

(a)

(b)

Fig. 7   Coils that were subjected to repeated thermal cycling: (a) 2-layer coil fabricated using the original procedure and (b) 4-layer coil fabricated using the improved procedure.

B. Thermal cycling tests

The primary performance metrics of a superconducting coil are the critical current I_c and n-value n, which respectively quantify the limit of direct current that the coil can carry before the coil becomes non-superconducting and the exponent describing how quickly the coil's voltage increases with direct current. In the absence of thermal runaway, the n-value depends on the level of uniformity in the superconductor. Therefore, these two performance metrics can be tracked to infer the health of the coil during thermal cycling. The critical current and n-value of the two coils shown in Figure 7 were measured at 77 K and self field** using the test rig depicted in Fig. 8. The key components of the rig are a dewar filled with liquid nitrogen, a linear amplifier capable of up to 120 A DC current, and a 6.5 digit multimeter. During a test, the DC current was slowly stepped up in small increments and a measurement was recorded at each step after holding the current long enough for the reading to stabilize. This hold duration was more than sufficient to overcome the charging delay of the uninsulated coil [18], which was < 1 s. The voltage taps are located about 10 cm away from each current lead to ensure that the measured current-transfer voltage at the critical current is less than 0.01% of the expected voltage at the critical current (based on 1 μV/cm electric field criteria) [19]. As shown in Fig. 8, each coil was mounted to a G10 plate that was suspended in the liquid nitrogen.

The testing procedure was the same as described in [13] except in the following ways. Here, the coils were given several minutes more time to warm up and were also given five minutes to cool down. Also, each coil was very slowly lowered into the liquid nitrogen bath instead of an abrupt dunk, which was determined to be overly aggressive. Lastly, the 6.5 digit multimeter was set to 100 averages to improve the measurement and provide a resolution of 0.1 μV.

**Self field is the magnetic excitation that a coil is exposed to due to its own current (i.e., when the coil is not subjected to any external magnetic fields).
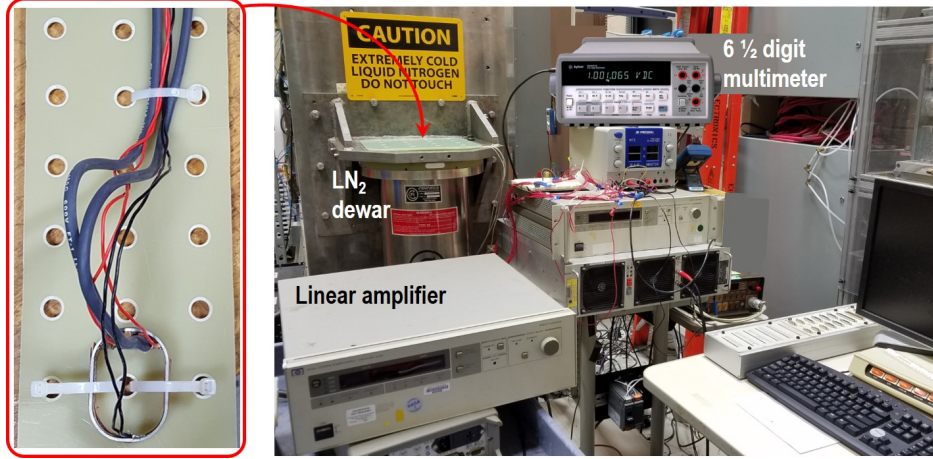
Fig. 8   NASA Glenn Research Center's high temperature superconducting coil test rig.

An electric field criteria (1 μV/cm) was used to define the critical current. The critical current and n-value of each curve was calculated by fitting the following function to the data using an unconstrained minimization algorithm,

$$\frac{V}{V_c} = \left(\frac{I}{I_c}\right)^n,$$

(1)

where V_c is the expected voltage at the critical current, which was calculated from the electric field criteria and the length of superconductor in the coil that is electrically located between the voltage taps. The change in the superconducting properties of each coil throughout thermal cycling is shown in Figure 9.

The critical current and n-value of each coil exhibit noticeable variation, but the variation is limited to a small range (less than about 1.5 A and about 3) and there is no apparent downward trend. Compared to the critical current, the variation in n-value is a considerably larger percentage of its average value. However, that metric is more sensitive to small errors in the data. A significant drop in the performance metrics of the 4-layer coil was observed after the eleventh thermal cycle, which indicated that damage had occurred between cycles nine and eleven. While obtaining a measurement after thirteen cycles, a current terminal de-bonded from the 4-layer coil. The terminal was soldered back onto the 4-layer coil after it was removed from the dewar and allowed to reach room temperature. The thermal cycling test was then continued for 5 more cycles. It can be seen that the superconducting performance of the 4-layer coil returned to its original level. This indicates that the drop in performance after cycle eleven was temporary and caused by a compromised electrical connection between the coil and a current terminal, rather than damage to the superconductor. This highlights the need to improve the quality and consistency of the solder joint between these two parts. In future coils, this solder joint will be created using an improved fixture that provides consistent pressure on the parts throughout the soldering process.

V. Conclusions

This paper presented the progress made over the past year toward a critical design of the superconducting rotor for NASA's high-efficiency megawatt motor (HEMM). Progress was made in both design and risk reduction testing. The design was refined by performing a more detailed analysis that eliminated two of the key simplifications used in the preliminary design phase. To approximate the assembled nature of the superconducting coils, the coil was modeled as an assembly of four individual, solid layer separated by thin plates rather than as a single, solid block of copper. To capture the thermally-induced stresses in the coil, a finite element simulation was conducted to solve for the rotor's thermal contraction due to a uniform cool down from room temperature to 60 K. The results of this simulation were used as the initial state of a structural simulation that applied the centrifugal loading. In this manner, the combined thermal and mechanical stress state of the rotor was evaluated. The original model was found to calculate the maximum von Mises stress in each component with sufficient accuracy. However, the improved thermal-structural model much more accurately captures the absolute deflection of the components and the stress in the end turns of the superconducting coil. Except for the dovetail retainer, the maximum von Mises stress in each component was found to be sufficiently
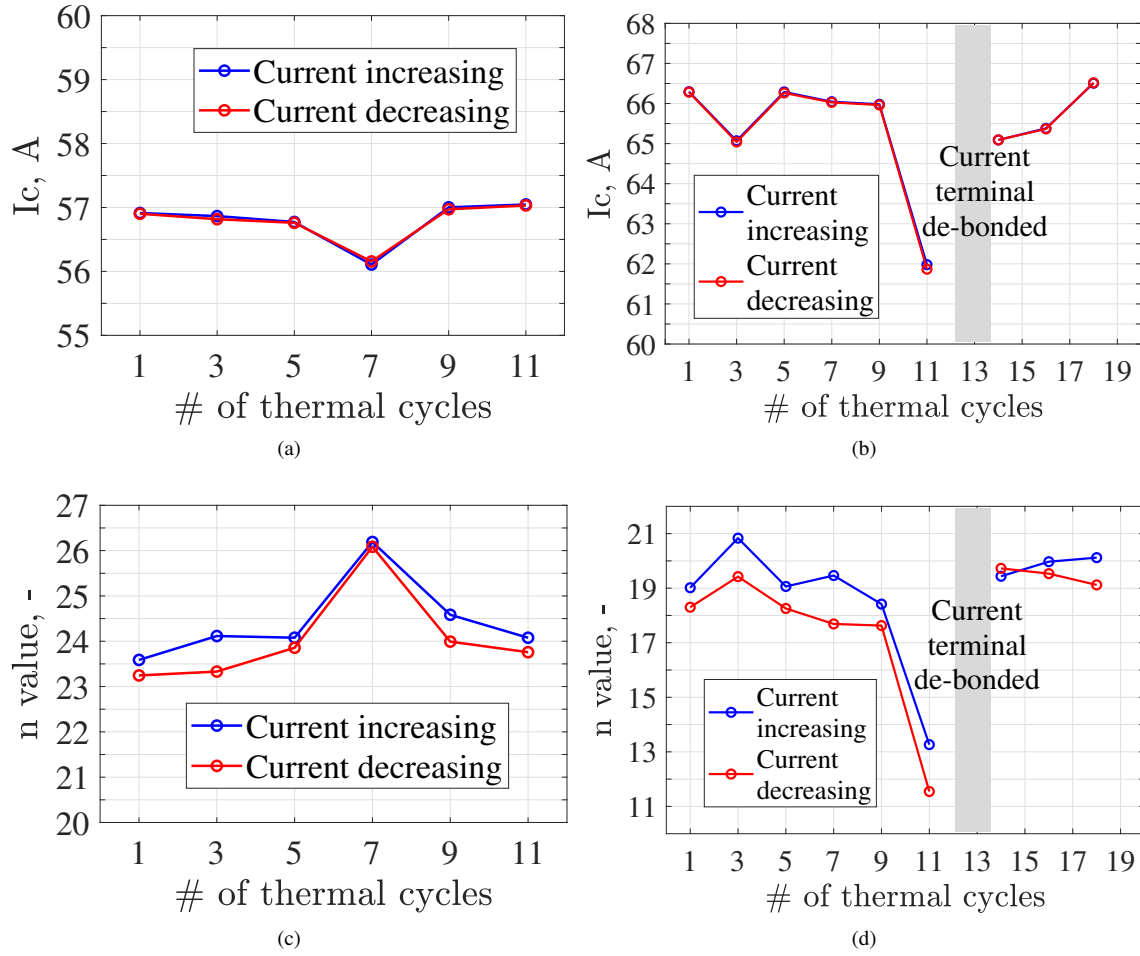
Fig. 9 Response of the test coils' superconducting properties to repeated thermal cycling between 77 K and room temperature: (a),(c) 2-layer coil fabricated using the original coil fabrication procedure and (b),(d) 4-layer coil fabricated using the improved coil fabrication procedure.

below the failure strength of the respective materials. The design of the dovetail retainer needs to be iterated by adding a fillet to eliminate a stress concentration. This simulation was also used to study the radial contraction of the rotor during cool down and subsequent radial expansion during a spin up to full speed. At operating temperature and full speed, the absolute radial position of the outermost point on the rotor was found to be 0.08 mm outward from the rotor's surface at room temperature. This result is important for properly sizing the air gap between the rotor and stator to ensure non-contact operation.

A collection of thermal cycling tests were performed on prototype coils to reduce the risks associated with thermal stresses. An improved coil fabrication procedure was described and depicted in detail. The improved procedure was used to fabricate several sub-scale coil. The response of two sub-scale coils to repeated thermal cycling between room temperature and liquid nitrogen temperature (77 K) was measured and presented. One coil was a 2-layer coil fabricated using the original coil fabrication procedure, whereas the other was a 4-layer coil fabricated using the improved procedure. The results highlighted the need to improve the repeatability of the solder joint between the current terminals and superconductor. Except for that issue, the data demonstrate that the proposed coil fabrication procedure can produce no-insulation, high temperature superconducting coils that can survive up to eighteen thermal cycles without apparent degradation.

Acknowledgments

References

[1] Jansen, R., Bowman, C., Jankovsky, A., Dyson, R., and Felder, J., "Overview of NASA Electrified Aircraft Propulsion (EAP) Research for Large Subsonic Transports," *53rd AIAA/SAE/ASEE Joint Propulsion Conference, AIAA Propulsion and Energy Forum, Atlanta, GA, AIAA 2017-4701*, 2017. doi:10.2514/6.2017-4701.

[2] Bradley, M. K., and Droney, C. K., "Subsonic Ultra Green Aircraft Research: Phase I Final Report," NASA Contractor Report, NASA/CR-2011-216847, 2011. URL `https://ntrs.nasa.gov/search.jsp?R=20110011321&hterms=NASA%2fCR-2011-216847&qs=N%3D0%26Ntk%3DAll%26Ntt%3DNASA%252FCR-2011-216847%26Ntx%3Dmode%2520matchallpartial`.

[3] Felder, J. L., Brown, G. V., DaeKim, H., and Chu, J., "Turboelectric Distributed Propulsion in a Hybrid Wing Body Aircraft," *20th International Society for Airbreathing Engines, ISABE-2011-1340, Gothenburg, Sweden*, 2011. URL `https://ntrs.nasa.gov/search.jsp?R=20120000856`.

[4] Bradley, M. K., and Droney, C. K., "Subsonic Ultra Green Aircraft Research: Phase 2. Volume 2; Hybrid Electric Design Exploration," NASA Contractor Report, NASA/CR-2015-218704/VOL2, 2015. URL `https://ntrs.nasa.gov/search.jsp?R=20150017039&hterms=NASA%2fCR-2015-218704%2fVOL2&qs=N%3D0%26Ntk%3DAll%26Ntt%3DNASA%252FCR-2015-218704%252FVOL2%26Ntx%3Dmode%2520matchallpartial`.

[5] Lents, C., Hardin, L., Rheaume, J., and Kohlman, L., "Parallel Hybrid Gas-Electric Geared Turbofan Engine Conceptual Design and Benefits Analysis," *52nd AIAA/SAE/ASEE Joint Propulsion Conference, AIAA Propulsion and Energy Forum, Salt Lake City, UT, AIAA 2016-4610*, 2016. doi:10.2514/6.2016-4610.

[6] Schiltgen, B. T., Freeman, J. L., and Hall, D. W., "Aeropropulsive Interaction and Thermal System Integration within the ECO-150: A Turboelectric Distributed Propulsion Airliner with Conventional Electric Machines," *16th AIAA Aviation Technology, Integration, and Operations Conference, AIAA AVIATION Forum, Washington, D.C., AIAA 2016-4064*, 2016. doi:10.2514/6.2016-4064.

[7] Welstead, J., and Felder, J. L., "Conceptual design of a single-aisle turboelectric commercial transport with fuselage boundary layer ingestion," *54th AIAA Aerospace Sciences Meeting, AIAA SciTech Forum, San Diego, CA, AIAA 2016-1027*, 2016. doi:10.2514/6.2016-1027.

[8] Perullo, C., Trawick, D., Armstrong, M., Tai, J. C., and Mavris, D. N., "Cycle Selection and Sizing of a Single-Aisle Transport with the Electrically Variable Engine(TM) (EVE) for Fleet Level Fuel Optimization," *55th AIAA Aerospace Sciences Meeting, AIAA SciTech Forum, Grapevine, TX, AIAA 2017-1923*, 2017. doi:10.2514/6.2017-1923.

[9] JDuffy, K. P., "Electric Motor Considerations for Non-Cryogenic Hybrid Electric and Turboelectric Propulsion," *51st AIAA/SAE/ASEE Joint Propulsion Conference, AIAA Propulsion and Energy Forum, Orlando, FL*, 2015.

[10] Jansen, R., Duffy, K. P., and Brown, G., "Partially turboelectric aircraft drive key performance parameters," *53rd AIAA/SAE/ASEE Joint Propulsion Conference, AIAA Propulsion and Energy Forum, Atlanta, GA, AIAA-2017-4702*, 2017, p. 4702. doi:10.2514/6.2017-4702.

[11] Jansen, R. H., Kascak, P., Dyson, R., Woodworth, A., Scheidler, J., Smith, A., Stalcup, E., Tallerico, T., De Jesus-Arce, Y., Avanesian, D., Duffy, K., Passe, P., and Szpak, G., "High Efficiency Megawatt Motor Preliminary Design," *2019 AIAA/IEEE Electric Aircraft Technologies Symposium (EATS)*, IEEE, 2019, pp. 1–13.

[12] Scheidler, J. J., "Preliminary Design of the Superconducting Rotor for NASA's 1.4 MW High-Efficiency Electric Machine," *2018 Joint Propulsion Conference*, 2018, p. 4617.

[13] Scheidler, J. J., and Tallerico, T. F., "Design, Fabrication, and Critical Current Testing of No-Insulation Superconducting Rotor Coils for NASA's 1.4 MW High-Efficiency Megawatt Motor," *2018 AIAA/IEEE Electric Aircraft Technologies Symposium (EATS)*, IEEE, 2018, pp. 1–9.

[14] Hahn, S., Park, D. K., Bascuñán, J., and Iwasa, Y., "HTS pancake coils without turn-to-turn insulation," *IEEE Transactions on Applied Superconductivity*, Vol. 21, No. 3, 2011, pp. 1592–1595. doi:10.1109/TASC.2010.2093492.

[15] Jordan, K., and Stoloff, N., "Plastic deformation and fracture in FeCo–2%V," *Trans. Met. Soc. AIME*, Vol. 245, 1969, pp. 2027–34.

[16] Lécrevisse, T., and Iwasa, Y., "A (RE)BCO pancake winding with metal-as-insulation," *IEEE Transactions on Applied Superconductivity*, Vol. 26, No. 3, 4700405, 2016, pp. 1–5. doi:10.1109/TASC.2016.2522638.

[17] Kim, J., Yoon, S., Cheon, K., Shin, K. H., Hahn, S., Kim, D. L., Lee, S., Lee, H., and Moon, S.-H., "Effect of resistive metal cladding of HTS tape on the characteristic of no-insulation coil," *IEEE Transactions on Applied Superconductivity*, Vol. 26, No. 4, 4601906, 2016, pp. 1–6. doi:10.1109/TASC.2016.2541687.

[18] Wang, X., Hahn, S., Kim, Y., Bascuñán, J., Voccio, J., Lee, H., and Iwasa, Y., "Turn-to-turn contact characteristics for an equivalent circuit model of no-insulation ReBCO pancake coil," *Superconductor Science and Technology*, Vol. 26, No. 3, 2013, p. 035012. doi:10.1088/0953-2048/26/3/035012.

[19] Ekin, J., *Experimental techniques for low-temperature measurements: cryostat design, material properties and superconductor critical-current testing*, p. 291, Oxford University Press, 2006.